

FINITE ELEMENT SIMULATION OF SHEAR AND COMPACT TENSION TESTS ON TIMBER

ELIŠKA ŠMÍDOVÁ*, PETR KABELE

Czech Technical University in Prague, Thákurova 7/2077, 166 29 Prague 6, Czech Republic

* corresponding author: eliska.smidova@fsv.cvut.cz

ABSTRACT. The non-linear finite element simulation of the ASTM shear and pre-stressed compact tension tests was conducted. Tested specimens were cut from the glued laminated timber made of European spruce (*Picea abies*) with the lamina thickness of 10.5 mm and 45 mm. The 2D homogeneous orthotropic constitutive model of the tensile-shear fracture in timber, which has been proposed by the authors, was used. The model calibration was adopted from the authors' recent experimental study. The numerical results show that the model can adequately reproduce both the experimental response and the crack pattern, which in certain cases comprises of cracking parallel or perpendicular to fibers. Furthermore, the results confirm that the value of the parameter f_{xy}^{ASTM} , obtained from ASTM shear test as the maximum attained force divided by the shearing area, represents the averaged stress at the failure plane, while the extreme stress experienced by the material is much higher.

KEYWORDS: ASTM shear test, pre-stress, compact tension test, glued laminated (GL) timber, tensile-shear fracture model, non-linear finite element analysis.

1. INTRODUCTION

The procedure for the determination of shear strength according to the standard ASTM D143-94 [1], see Figure 2, is widely accepted and used for timber and wood products. However, as shown by numerical simulations by Sajdlová and Kabele [2], the stress distribution along the failure plane in such shear-test configuration is non-uniform with strong concentrations at the edges of the loading platens.

As reported in [3], the compact tension (CT) test on pre-stressed specimens with reduced ligament depth was conducted with the primary aim of obtaining the fracture behavior in the crack-normal direction for the fibers' rupture concentrated around or at the cross-section ahead of the notch. Nevertheless, such failure type occurred only in one case out of five accompanied by fiber bundles' disintegration propagating along the grain. In the rest of the specimens, various failure types with fibers' rupture or disintegration or their combinations were observed. The authors recommended only qualitative interpretation of the obtained results due to low precision of prescribed strain, presence of disintegration propagating along the grain that accompanied fibers' rupture, role of lateral compression in fibers' rupture, or insufficient number of specimens for each failure type.

The aim of this study is to conduct a numerical simulation of (i) the ASTM shear test and (ii) the pre-stressed CT test on glued laminated timber (GLT) specimens and analyse the behavior of the tensile-shear crack parallel or perpendicular to the grain. To this end, the material model of the tensile-shear fracture in timber implemented in finite element method is used.

2. CONSTITUTIVE MODEL

We briefly review the material model of tensile-shear fracture in timber that the authors' team has recently developed and implemented in a FEM code [4]. Timber is considered as a 2D homogeneous continuum. The model aims at capturing fracture under tension, shear, and their combination, while taking into account the phenomena of the elastic and inelastic behavior in a small deformation range, material orthotropy, both in linear and non-linear range, cracking across and along fibers, and the behavior under unloading/reloading. Non-linear response under combination of compression and shear is considered as a perfectly plastic.

The model for the nonlinear behavior is composed of:

- (i) failure criterion defining the stress condition for crack initiation,
- (ii) crack-type criterion that distinguishes whether the crack occurs across or along the fibers,
- (iii) cohesive (traction-separation) law defining the response of a crack.

Failure (fracture) is assumed to occur when the following condition is satisfied:

$$F(\sigma_x, \sigma_y, \tau_{xy}) = 1 \quad (1)$$

Here σ_x , σ_y , and τ_{xy} are the stress components with respect to the axes of orthotropy. The failure function F is defined by the Tsai-Hill formulation [5] as:

$$F = \frac{\sigma_x^2}{f_x^2} + \frac{\sigma_y^2}{f_y^2} + \frac{\tau_{xy}^2}{f_{xy}^2} - \frac{\sigma_x \sigma_y}{f_x^2} \quad (2)$$

$$\text{if } \sigma_x \geq 0 \text{ then } f_x = f_{tx} \text{ else } f_x = f_{cx} \quad (3)$$

$$\text{if } \sigma_y \geq 0 \text{ then } f_y = f_{ty} \text{ else } f_y = f_{cy} \quad (4)$$

where f_{xy} is the absolute value of the shear strength. Symbols f_x and f_y are tensile or compressive strength along and across the fibers, respectively: for the positive values of σ_x and σ_y , the strengths f_x and f_y correspond to the tensile strength values f_{tx} and f_{ty} , respectively, otherwise the compressive strength values f_{cx} and f_{cy} are adopted.

The crack-type criterion is based on the consideration that when timber is exposed to tension in the direction parallel or nearly parallel to the grain, rupture occurs across the grain and the crack is perpendicular to the principal stress direction. When the angle θ , describing the deviation of the principal tension from the grain, is larger than a certain threshold (θ_c), then the crack forms along the grain regardless of the principal stress direction. To distinguish these cases, the crack-type function F_{CT} , Eq. 5, and criteria for cracking across and along the fibers, Eq. 6 and Eq. 7, are introduced:

$$F_{CT} = \left| \frac{2\tau_{xy}}{\sigma_x - \sigma_y} \right| - \tan(2\theta_c) \quad (5)$$

$$\text{Crack across the grain: } F_{CT} < 0 \quad (6)$$

$$\text{Crack along the grain: } F_{CT} \geq 0 \quad (7)$$

In the 2D stress space the crack-type function F_{CT} defines a plane, which divides the failure surface into two parts.

The concept of the cohesive crack model [6] is used to model the material response after failure. The bridging effect of incompletely ruptured or delaminated fibers is represented by a cohesive traction acting between the crack faces. The traction-separation law defines the relation between the normal and tangent tractions t_n and t_m and the relative normal and tangent displacement between the crack surfaces δ_n and δ_m . The exponential form of the traction-separation law originally proposed by Hordijk [7] was adapted in the present model as:

$$t_n(\delta_n, \delta_m) = \begin{cases} t_n^{ci} \left(1 - \sqrt{\frac{\delta_n^2}{\delta_{n,crit}^2} + \frac{\delta_m^2}{\delta_{m,crit}^2}} \right) \left(1 + \left(\frac{c_1 \delta_n}{\delta_{n,crit}} \right)^3 \right) \exp\left(\frac{c_2 \delta_n}{\delta_{n,crit}} \right) - \exp(-c_2) \left(1 + c_1^2 \right) \frac{\delta_n}{\delta_{n,crit}} & \text{for } \delta_n \in [0, \delta_{n,crit}) \\ & \text{and } \delta_m \in [0, \delta_{m,crit}) \\ 0 & \text{for } \delta_n \geq \delta_{n,crit} \text{ or } \delta_m \geq \delta_{m,crit} \end{cases} \quad (8)$$

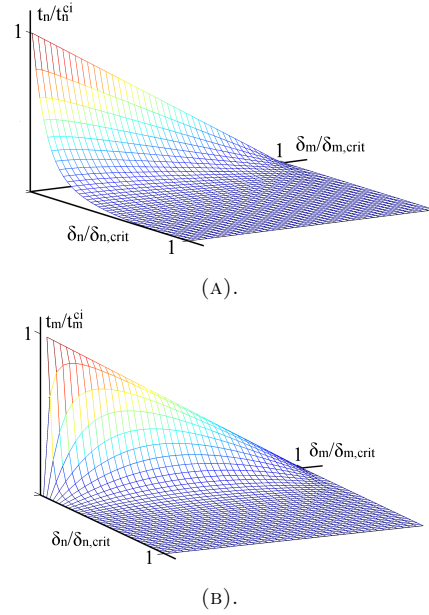


FIGURE 1. Cohesive law in (A) crack-normal direction $t_n(\delta_n, \delta_m)$ with fracture energy G_f as an integral of $t_n(\delta_n, \delta_m)$ and (B) crack-tangent direction $t_m(\delta_n, \delta_m)$ [4].

$$t_m(\delta_n, \delta_m) = \begin{cases} t_m^{ci} \left(1 - \sqrt{\frac{\delta_n^2}{\delta_{n,crit}^2} + \frac{\delta_m^2}{\delta_{m,crit}^2}} \right)^{\frac{2}{\pi}} \arctan \left(\frac{\delta_m}{l_{ch}} \frac{1 - \left(\frac{\delta_n}{\delta_{n,crit}} \right)^p}{\left(\frac{\delta_n}{\delta_{n,crit}} \right)^p} \right) & \text{for } \delta_n \in [0, \delta_{n,crit}) \\ & \text{and } \delta_m \in [0, \delta_{m,crit}) \\ 0 & \text{for } \delta_n \geq \delta_{n,crit} \text{ or } \delta_m \geq \delta_{m,crit} \end{cases} \quad (9)$$

where t_n^{ci} is the crack-normal traction at crack initiation, t_m^{ci} is the crack-tangent traction at crack initiation, c_1 and c_2 are fitting parameters defining the slope of the t_n function, $\delta_{n,crit}$ and $\delta_{m,crit}$ are the values of normal and shear displacement jump at which the cohesive traction diminishes to zero, l_{ch} is the characteristic length of the smeared crack model (the width of the fracture process zone), and p is a material parameter that determines the slope of the function t_m . The same form of the traction-separation relation is used both for cracks along and across the grain, although the respective values of the parameters may be different. The plot of traction-separation law is shown in Figure 1.

3. MODEL CALIBRATION

The tensile-shear fracture model has already been calibrated within authors' recent experimental study [3]. To this end, experimental results from off-axis tensile and compressive tests and compact tension test were used. The parameters applicable to the states before failure, such as the elastic moduli (E_x ,

Parameter	Unit	<i>Avg</i>
E_x	[MPa]	12418.0
f_x	[MPa]	77.6
E_y	[MPa]	371.0
f_y	[MPa]	3.2
ν_{xy}	[-]	0.37
ν_{yx}	[-]	0.01
G_{xy}	[MPa]	310.0
$E_{c,x}$	[MPa]	16142.0
$f_{c,x}$	[MPa]	56.3
$E_{c,y}$	[MPa]	310.0
$f_{c,y}$	[MPa]	3.3
f_{xy}^{ASTM}	[MPa]	3.7

TABLE 1. Off-axis tension and compression and shear test results for 10.5 mm GLT where *Avg* is the mean (values adopted from [3]).

E_y , G_{xy}) and Poisson's ratios (ν_{xy} , ν_{yx}), are listed in Table 1. In this section, we briefly review the parameters obtained by the calibration of the failure-related model components.

The failure surface is defined by five parameters: the uniaxial tensile and compressive strengths along and perpendicular to the grain (f_x , f_{cx} , f_y , f_{cy} , resp.) and the shear strength (f_{xy}). The values of tensile and compressive strengths were directly retrieved from the tensile and compressive tests. They are listed in Table 1. The parameter f_{xy} was obtained by the least-square fitting of the failure criterion, expressed using an uniaxial failure function defining the relation between the axial stress at failure σ_{axial} and the off-axis angle θ , to the failure data from tensile and compressive tests. This procedure yielded $f_{xy} = 8.5$ MPa [3].

With the crack-type criterion, the parameter of the critical load-grain angle θ_c is introduced in the model to distinguish the cases when failure occurs across or along the grain. Based on visual inspection of tensile specimens that failed due to fibers rupture, it was found that the actual grain deviation from the load direction is in the interval of $[0^\circ, 2^\circ]$. Opposed to the recent numerical simulation analysis [8], we set $\theta_c = 1.6^\circ$ to enable cracking both parallel and perpendicular to the grain.

The traction-separation relationship t_n vs. δ_n for the crack along the grain was obtained by the inverse analysis of the compact tension (CT) tests results [9]. The inverse analysis was applied on three load vs. crack mouth opening displacement curves, which corresponded to the minimum, intermediate, and maximum measured response. Corresponding values of parameters in Table 2 are denoted accordingly.

CT test	Cohesive law				
	Fit response	t_n^{ci} [MPa]	$\delta_{n,crit}$ [mm]	c_1 [-]	c_2 [-]
Minimum		3.6	0.52	8.8	21.5
Intermediate		3.8	0.18	1	3.7
Maximum		5.3	0.20	1.0	3.7

TABLE 2. Values of the cohesive law parameters for the crack along the grain calibrated to the results of inverse analysis for the minimum, intermediate, and maximum response of the CT test results (transcribed from [3]).

4. SHEAR TEST AND PRE-STRESSED COMPACT TENSION TESTS

4.1. MATERIAL

The specimen for the ASTM shear test [1] was a notched block saw-cut from larger pieces of glued laminated timber (GLT) made of European spruce (Picea abies) with the lamina thickness of 10.5 mm. The dimensions and configuration are depicted in Figure 2.

The compact tension (CT) specimens were cut from larger pieces of European spruce GLT with the lamina thickness of 45 mm with the load-grain angle $\theta = 0^\circ$. The specimen size and test set-up are shown in Figure 5A.

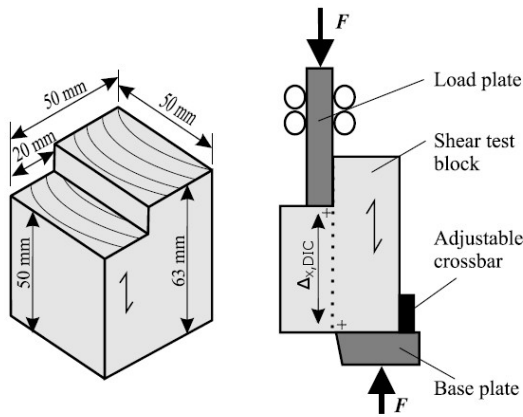
Both samples were fabricated to be representative elements of the GLT structure and free of defects such as knots or cracks. The tested specimens were conditioned in an indoor environment with a temperature of 21° and relative humidity of 55% for 2 months. During testing, the average moisture content of the samples was 8% and the density was 463 kg/m^3 .

4.2. EQUIPMENT AND DATA ACQUISITION

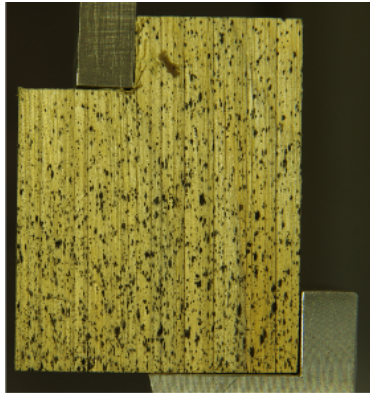
The shear and compact tension tests were conducted in MTS Alliance RT/30 electromechanical testing machine equipped with a 30 kN load cell. Force and crosshead displacement were recorded at 10 Hz. Image data were collected for a subsequent digital image correlation (DIC) analysis with snapshots taken every 5 sec using Canon EOS 70D 20 megapixel digital camera fitted with Canon EF 100 mm $f/2.8$ lens. The camera and data logger records were synchronized so as to link the photographs with the applied load. The Ncorr v. 1.2 open-source software [10] with the Ncorr_post in-house graphical interface [11] were involved to run the DIC analyses.

4.3. SHEAR TEST

The shear test set-up was conducted according to the standard ASTM D143-94 [1], see Figure 2. The specimens were freely laid on the steel base plate without capping or gluing. No extensometer was attached and the vertical relative displacements $\Delta_{x,DIC}$ depicted in Figure 2A were acquired from DIC measurements.



(A).



(B).

FIGURE 2. Shear-parallel-to-grain test according to the standard ASTM D143-94: (A) set-up and relative vertical displacement $\Delta_{x,DIC}$ calculated by DIC analysis, (B) a mounted specimen. [3]

The load was applied with the crosshead displacement control at a rate of 0.6 mm/min.

The valid specimens failed as the plane defined by the inner edge of the base plate and the inner corner of the notch sheared off in the direction parallel to the grain. The specimens with the fracture plane extended back onto the supporting surface e.g. due to material imperfections were ignored, since this failure is governed by the compressive resistance between the load and support plates, rather than by shear.

We calculated the shear strength parameter f_{xy}^{ASTM} according to the standard ASTM D143-94 [1] as:

$$f_{xy}^{ASTM} = \frac{F_{max}}{A} \quad (10)$$

where F_{max} is the maximum attained force, and A is the shearing area. As seen in Figure 2 the design shearing area is 2500 mm². The actual size of this area was calculated using the measured dimensions of each specimen.

The Figure 3 shows the valid responses as load vs. relative vertical displacement. For the curve S1, the peak value can be clearly identified and it is followed by a decrease and hardening. Compared to it, the

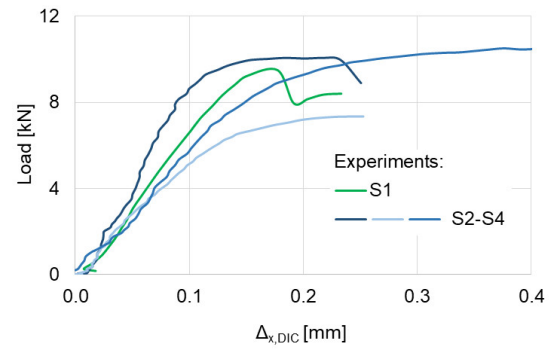


FIGURE 3. Results of the shear-parallel-to-grain test according to the standard ASTM D143-94 [1]: load vs. DIC relative vertical displacement $\Delta_{x,DIC}$. [3]

curves S2-S4 exhibit plateau. Despite not being plotted in this figure, all the curves S1-S4 end with sudden drops, which are associated with an unstable fracture propagation. The Table 1 lists the obtained values of the shear strength f_{xy}^{ASTM} .

The specimens failed with the crack parallel to the grain more or less along the expected shearing area. The crack of the specimen S1 was slightly skewed heading from the inner edge of the notch towards the inner edge of the bottom support, see Figure 4A. Compared to it, the cracks of the specimens S2-S4 were almost aligned with the specimens' longer edges spreading from the inner edge of the notch, see Figure 4B.

4.4. PRE-STRESSED COMPACT TENSION TEST

The outer dimensions and loading of the CT specimen were based on the ASTM E1820-09 standard [12]. To induce the fiber rupture propagating along the ligament and obtain the fracture behavior in the crack-normal direction, the test arrangement was modified with (i) pre-stress $\Delta\sigma_{y_a}$ between 2.7 MPa and 3.3 MPa (Figure 5A) and (ii) reduction of the ligament depth to 10 mm (Figure 5B). The load was applied with the crosshead displacement control at a rate of 0.5 mm/min.

All five specimens failed with various failure types. Two specimens failed with the failure type F0 - disintegration parallel to the grain initiated at or around the notch tip where the crack propagated perpendicular to the ligament, see Figure 6A. The failure type F1, in which fibers rupture is concentrated around or at the cross-section ahead of the notch (Figure 6B), occurred once. Two specimens exhibited the failure type F2, in which fibers' rupture concentrated around or at the cross-section ahead of the notch was either followed by disintegration along the grain propagating from the cross-section's middle, denoted as F2-a (Figure 6C), or accompanied by disintegration propagating from both the notch tip and the cross-section's middle, denoted as F2-b (Figure 6D).

The recorded load vs. crosshead displacement responses are presented in Figure 7. Their differences

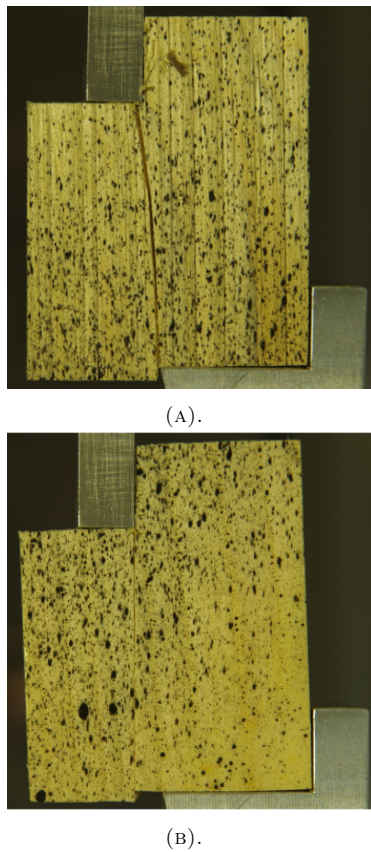


FIGURE 4. The final fracture of the shear-parallel-to-grain test according to the standard ASTM D143-94: (A) the specimen S1 and (B) the specimen S3.

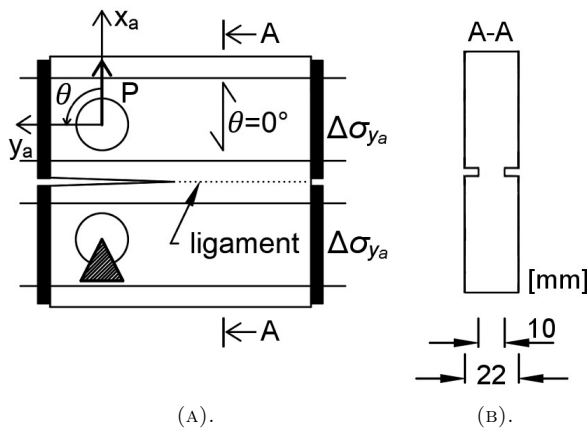


FIGURE 5. Pre-stressed compact tension (CT) test with the load-grain angle $\theta = 0^\circ$: configuration and dimensions. (A) Front view. (B) Side view. [3]

in shape reflected various failure types that occurred. All five curves were linear at the beginning. Two curves with failure type F0 proceeded with hardening branch and a final drop. In one curve exhibiting failure type F1, softening branch with little drops and hardening portions followed. In the curve with failure type F2-a, the softening and then hardening branches followed. After the linear branch, the curve with failure type F2-b captured a decrease in slope, softening, and hardening.

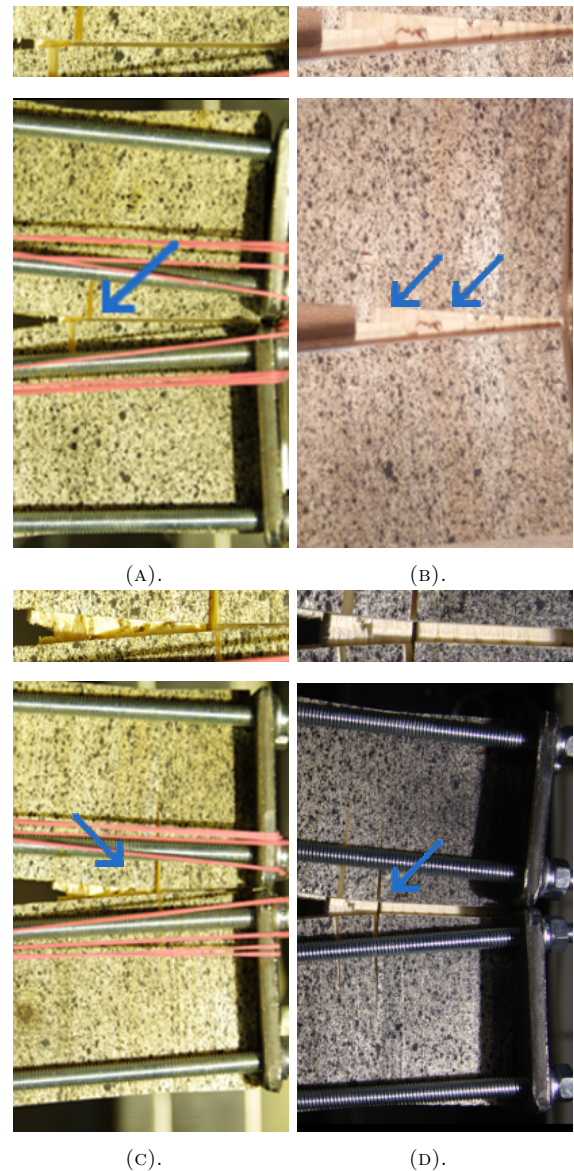
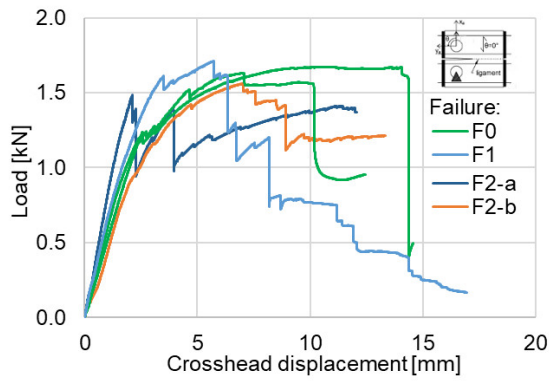


FIGURE 6. Failure of pre-stressed CT specimens with the load-grain angle of $\theta = 0^\circ$: (A) type F0 - disintegration parallel to the grain initiated at or around the notch tip, (B) type F1 - fibers' rupture concentrated around or at the cross-section ahead of the notch, (C) type F2-a - fibers' rupture concentrated around or at the cross-section ahead of the notch followed by disintegration propagating from the cross-section's middle, and (D) type F2-b - fibers' rupture concentrated around or at the cross-section ahead of the notch accompanied by disintegration propagating from both the notch tip and the cross-section's middle. [3]

5. NUMERICAL SIMULATIONS OF SHEAR TEST

5.1. INTRODUCTION

The aim of the ASTM shear test simulations was to demonstrate the capability of the constitutive model outlined in Section 2 to reproduce the behavior of timber dominated by shear crack parallel to the grain. As the critical crack-sliding displacement $\delta_{m,crit}$ for



(A).

FIGURE 7. Load vs. crosshead displacement for pre-stressed CT specimens with the load-grain angle of $\theta = 0^\circ$ that failed in modes F0, F1, and F2. [3]

the crack parallel to the grain is not known from the model calibration reviewed in Section 3, numerical simulations were run with different values from an estimated range. The mesh used for discretization of the timber shear blocks (Figure 8) was regular consisting of four-node quadrilateral plane-stress elements with the size of approx. 2.5 mm by 2.5 mm. Only the elements along the shearing line had the width of 2.0 mm, which was used as the characteristic length parameter l_{ch} for the crack parallel to the grain. As the material was orthotropic, the material axes were assigned to each element so as the grain direction was parallel to the specimen longitudinal direction. The vertical displacement U_y with the unit magnitude of $U_y^0 = 0.1$ mm was prescribed in half of the nodes along the horizontal notch edge, except for the inner corner node enabling shearing of the column of elements. This unit load magnitude was scaled by an appropriate incremental loading factor, see Section 5.2. The vertical load plate that prevents the specimen from rotation was modelled as prescribed supports $U_x = 0$ mm along the vertical notch edge. Similarly, the base plate and the crossbar were considered as the supports $U_y = 0$ mm and $U_x = 0$ mm, respectively. The zero vertical displacement was prescribed only in the nodes placed further from the base plate - crossbar corner to minimize the effect of friction. The material-nonlinear calculations were performed using the Newton-Raphson method.

5.2. NUMERICAL SOLUTION ASPECTS

The element size and loading increment magnitude were determined by the numerical analyses of two models with meshes with typical element size of 2.5 mm and 1.0 mm. The mesh with 2.5 mm element size was used to compare the incremental loading factor of 0.15 and 0.30, that is the actual load increment of 0.015 mm and 0.030 mm, respectively. The results in Figure 9 show that the load-relative displacement curves are similar for both models up to the relative displacement of $\Delta_{x,DIC} = 0.175$ mm, where the finer

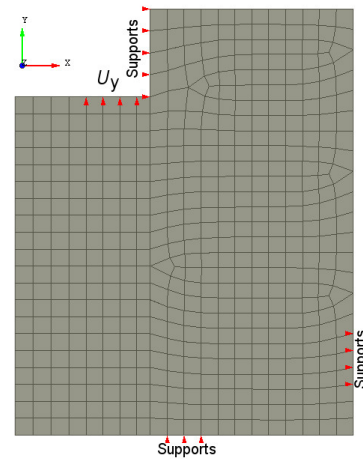


FIGURE 8. 2D FE mesh composed of approx. 2.5 mm by 2.5 mm quadrilaterals aligned with the specimen longitudinal direction and lamina.

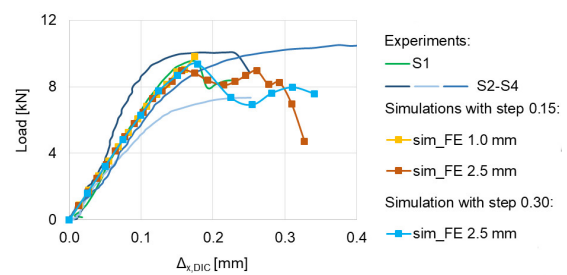


FIGURE 9. The effect of element size and load step size on calculated response in the shear test simulation.

mesh calculation was ended due to exceeded convergence criteria. The obtained fracture patterns were also similar: the crack parallel to the grain spread from the notch edge downwards along the shearing line towards the compression-shear zone with non-linear deformation around the edge of the bottom support. A conclusion was drawn to be used for all the subsequent analyses, that the mesh with the 2.5 mm element size provided a converged solution. Comparing the calculation results with the incremental loading factor of 0.15 and 0.30, we can see a good agreement in responses and crack patterns.

5.3. RESULTS

First, in Figure 10, we compare the experimental results with the numerical responses obtained with the intermediate parameters in Table 2 for different values of critical crack-sliding displacement $\delta_{m,crit} = \{0.03, 0.055, 0.100, 0.600\}$ mm. We can see, that the model reproduces well the initial slope, the post-peak branch, and the lowest, intermediate, and the highest level of the load capacity observed in tests. We can notice, that the results with $\delta_{m,crit} = \{0.100, 0.600\}$ mm yield almost the same response and the parameter $\delta_{m,crit} \geq 0.100$ mm does not influence the responses.

Second, in Figure 11, we compare the experimental

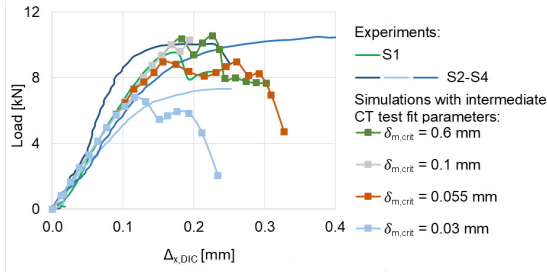


FIGURE 10. Load vs. DIC relative vertical displacement $\Delta_{x,DIC}$ for the results of ASTM shear test experiments and simulations calculated with the intermediate parameters from Table 2 and different values of $\delta_{m,crit}$.

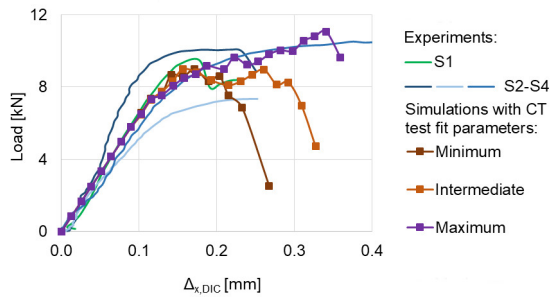


FIGURE 11. Load vs. DIC relative vertical displacement $\Delta_{x,DIC}$ for the results of ASTM shear test experiments and simulations calculated with the minimum, intermediate, and maximum parameters from Table 2 and $\delta_{m,crit} = 0.055$ mm.

results with the numerical responses obtained with $\delta_{m,crit} = 0.055$ mm and the minimum, intermediate, and maximum parameters from Table 2. The calculations with the minimum and the intermediate parameters reproduce well the S1 experiment, as for the peak value followed by a decrease, hardening and a final drop. They differ only in the final drops that occur beyond $\Delta_{x,DIC} = 0.2$ mm and $\Delta_{x,DIC} = 0.26$ mm, respectively. Compared to it, the calculation with the maximum parameters reproduce well the S2 and S4 experiment exhibiting the plateau followed by the final drop.

As expected, a similar crack pattern occurred in the numerical simulations: the crack parallel to the grain initiated under tensile-shear stress states at the upper edge of the shearing area propagating downwards. A zone, in which the non-linear deformation was developing under compression and shear, spread upward from the lower support along the shear plane until it reached the downward-growing crack, see Figure 12A. The final strain states ε_{xx} and γ_{xy} are shown in Figure 12B and Figure 12C, respectively. Comparing the strain states with the image of cracking at the maximum relative vertical displacement in Figure 4, we can see, that the model captures the crack pattern adequately.

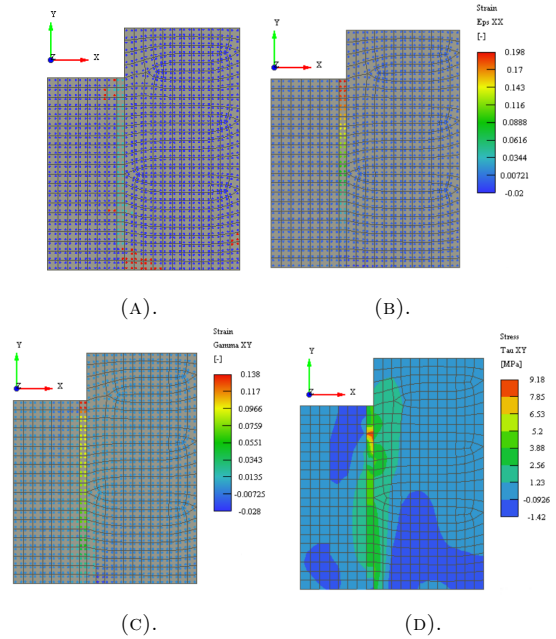


FIGURE 12. ASTM shear test simulation result at (A-C) $\Delta_{x,DIC} = 0.3$ mm and (D) $\Delta_{x,DIC} = 0.16$ mm for intermediate parameters from Table 2 and $\delta_{m,crit} = 0.055$ mm: (A) crack parallel to the grain (red) and non-linear deformation zone (green) developed under compression and shear stress states, (B) normal strain ε_{xx} , (C) shear strain γ_{xy} , and (D) shear stress τ_{xy} .

As overviewed in Section 4.3, the shear strength according to the ASTM standard f_{xy}^{ASTM} is calculated by dividing the maximum attained force F_{max} and the shearing area A . Therefore, it corresponds to the average shear stress on the area at the specimen failure. The Figure 12D shows the shear stress along the shearing area around the peak load at $\Delta_{x,DIC} = 0.16$ mm.

6. NUMERICAL SIMULATIONS OF PRE-STRESSED CT TEST

6.1. INTRODUCTION

The main objectives of the pre-stressed CT test simulations were to demonstrate the capability of the constitutive model outlined in Section 2 to reproduce the behavior of timber dominated by tensile crack parallel or perpendicular to the grain or combination of both, i.e., the failure modes F0-F2. Based on the results from Section 5.3, the parameter $\delta_{m,crit} = 0.055$ mm for the crack along the grain was used in pre-stressed CT test simulations. As the cohesive law parameters for the crack across the grain are not known from the model calibration reviewed in Section 3, numerical simulations were run with assumed values of critical crack opening and sliding displacements $\delta_{n,crit}^{across} = 1.1$ mm and $\delta_{m,crit}^{across} = 1.1$ mm, and parameters $c_1^{across} = 3.0$ and $c_2^{across} = 6.7$.

The pre-stressed CT specimens were discretized with a regular mesh consisting of four-node quadrilateral plane-stress elements with the size of approx.

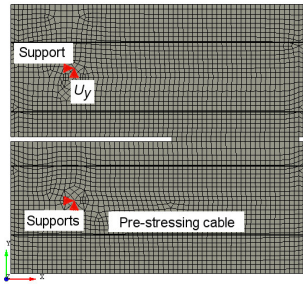


FIGURE 13. 2D FE mesh composed of approx. 2.0 mm by 2.0 mm quadrilaterals aligned with the specimen edges.

2.0 mm by 2.0 mm (to model the specimen and confinement plattens) and four external cable elements (to induce the confinement), see Figure 13. The axes of the orthotropic timber material were assigned to each element so as the grain direction was perpendicular to the direction of the specimen's notch.

The loading was applied as the vertical displacement U_y with the unit magnitude of $U_y^0 = 0.01$ mm to the upper loading hub as shown in Figure 13. This unit load magnitude was scaled by an incremental loading factor specified in Section 6.2. The loading point was placed at a small vertical offset of 4 mm from the loading hub's centroid to enhance the non-symmetric failure as observed in the experiments. The bottom hub was fixed at its center. The material-nonlinear calculations were performed using the Newton-Raphson method.

6.2. NUMERICAL SOLUTION ASPECTS

Using two models with meshes with typical element size of 2.0 mm and 1.0 mm, the appropriate element size and loading increment magnitude were determined. The mesh with 2.0 mm elements was used to run calculations with the incremental loading factor of 50 and 35, that is the actual load increment of 0.50 mm and 0.35 mm, respectively. As seen in Figure 14, the load-crosshead displacement curves were similar for both models up to the displacement of 3.0 mm, where the calculation with the finer mesh ended due to exceeded convergence criteria. The obtained fracture patterns were similar, both of the type F1 - fibers' rupture concentrated around or at the cross-section ahead of the notch. It was concluded that the mesh with 2.0 mm element size provided a converged solution and, thus, can be used for all subsequent calculations. Comparing the calculation results with the incremental loading factor of 50 and 35, we can see a good agreement in responses in Figure 14 and the same can be said about the crack patterns. The slight difference in slope of the softening branches is attributed to the fact that the disintegration of the fibers' bundles, that accompanied fibers' rupture along the ligament within the failure type F1, occurred at different locations and had a different extent in

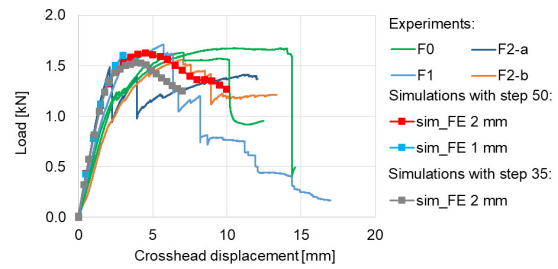


FIGURE 14. The effect of element size and load step size on calculated response in the CT test simulation with the pre-stress of 3.3 MPa, $\theta_c = 1.6^\circ$, and failure type F1.

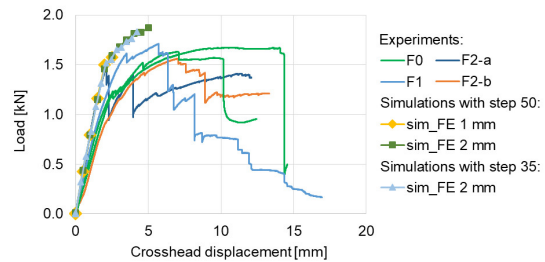


FIGURE 15. The effect of element size and load step size on calculated response in the CT test simulation with the pre-stress of 3.3 MPa, $\theta_c = 0.4^\circ$, and failure type F0.

each calculation.

To confirm that the element size of 2.0 mm and the loading increment of 0.50 mm are also suitable for other failure types, numerical analysis similar to the previous one (Figure 14) was conducted with the critical load-grain angle of $\theta_c = 0.4^\circ$ which hindered propagation of the main crack across the grain in the notch direction and encouraged failure due to vertical cracking along the grain (type F0) - see also the discussion in Section 6.4. The results in Figure 15 show that both models yielded similar response up to the displacement of 2.5 mm, where the finer mesh calculation ended due to exceeded convergence criteria. The obtained fracture patterns were very similar, both categorized as failure type F0. The comparison of the simulations with the incremental loading factor of 50 and 35 showed a very good agreement in responses and crack patterns.

6.3. RESULTS

Results of the calculations with pre-stress levels of 3.3, 3.0, 2.7, and 2.1 or 1.0 MPa are summarized in Figure 16 and Figure 17. Figure 17 displays the normal strains ε_{xx} and ε_{yy} . Concentrations of these strains occur due to opening of horizontal (ε_{yy}) or vertical (ε_{xx}) cracks; therefore their contour plots indicate the crack patterns, which can be compared with those observed in experiments and shown in Figure 6.

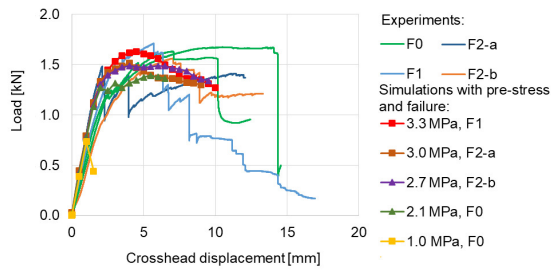


FIGURE 16. Load vs. crosshead displacement for the results of CT test experiments and simulations calculated with $\theta_c = 1.6^\circ$ and different pre-stress levels.

In the simulation with pre-stress of 3.3 MPa we observed propagation of a major crack across fibers in the direction of the notch (Figure 17A top) with multiple short branches along the grain (Figure 17A bottom). This pattern corresponds well with the failure type F1 seen in Figure 6B. The respective load-displacement curve (Figure 16) exhibits the highest peak and post-peak softening. In the simulation with 3.0 MPa, crack across fibers propagated in the direction of the notch up to approx. one third of the ligament's length (Figure 17B bottom) from where crack along the grain started to propagate (Figure 17B top). Such a cracking corresponds to failure type F2-a shown in Figure 6C. The calculated load-displacement response (Figure 16) reaches the second highest peak, out of the curves for different pre-stress levels, followed by post-peak softening, hardening, and then a decrease at the end. In the simulation with 2.7 MPa, a major crack across fibers (Figure 17C bottom), that propagated in the direction of the notch, was accompanied by the first branch along fibers (initiated at the notch tip) and followed by the second branch along fibers (initiated at approx. one half of the ligament's length), see Figure 17C top. This cracking resembled failure type F2-b shown in Figure 6D. The obtained load-displacement curve (Figure 16) has the third highest peak followed by post-peak softening, hardening, and a decrease at the end. Crack along the grain initiated at or around the notch tip dominated in the calculations with 2.1 MPa and 1.0 MPa (Figure 17D top). Nevertheless, it was accompanied by crack across the grain in a few finite elements at the ligament's beginning (Figure 17D bottom) with crack-normal strain (i.e. ε_{yy}) much lower than that of crack along the grain (i.e. ε_{xx}). Such failure was considered comparable to failure type F0 presented in Figure 6A. The obtained load-displacement curves are shown in Figure 16 with the fourth and fifth highest calculated peak. For the calculation with 2.1 MPa, the peak is followed by post-peak hardening and a decrease at the end. For the simulation with 1.0 MPa, the post-peak branch is softening.

It is obvious that the numerical calculations were able to reproduce the different failure patterns (F0-F2) observed in the experiments. The models also

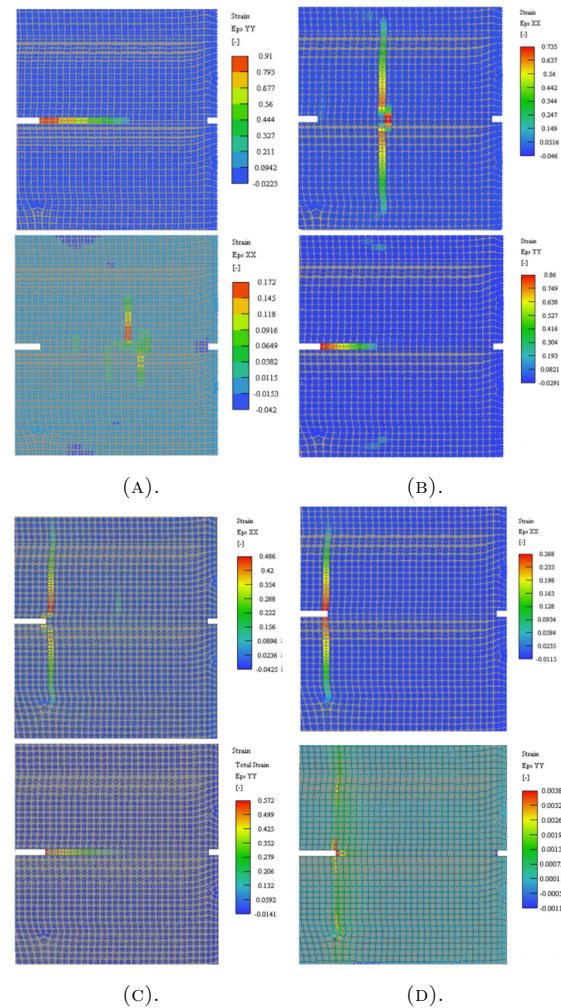


FIGURE 17. Distributions of normal strains ε_{xx} and ε_{yy} obtained from the CT test simulations with different pre-stress levels: (A) pre-stress 3.3 MPa (state at $U_y = 7.0$ mm), (B) pre-stress 3.0 MPa (state at $U_y = 9.0$ mm), (C) pre-stress 2.7 MPa (state at $U_y = 7.0$ mm), and (D) pre-stress 1.0 MPa (state at 1.5 mm).

captured well the initial slope, the peak, and the post-peak trends of the load-displacement records.

6.4. EFFECT OF THRESHOLD ANGLE θ_c

The value of the threshold angle θ_c , which determines if a crack forms across the grain (splinter failure) or along grain, could not be exactly determined from uniaxial tension tests [3]. The tests only indicated that it falls within the range between 0° and 2° . Therefore, to investigate how sensitive is the model of the CT test to this parameter, two more sets of calculations were run with different values of $\theta_c = 0.4^\circ$ and $\theta_c = 1.4^\circ$. Results are summarized in Figure 18 and Figure 19.

In both sets of simulations with pre-stress of 1.0 MPa - 3.3 MPa, we observed a major crack along the grain initiated at or around the notch tip (Figure 19 top), that was accompanied by a short branch, which propagated from the notch tip in the direction of the notch, either as crack along the grain for $\theta_c = 0.4^\circ$

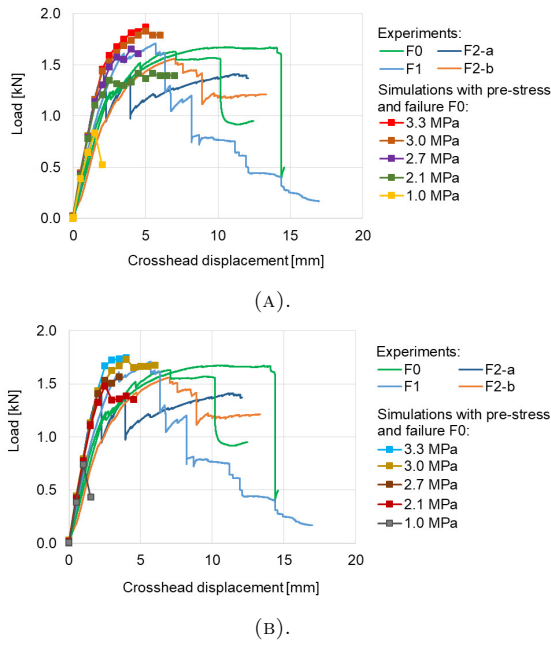


FIGURE 18. Load vs. crosshead displacement for the results of CT test experiments and simulations calculated for different pre-stress levels with (A) $\theta_c = 0.4^\circ$ and (B) $\theta_c = 1.4^\circ$ leading to failure type F0.

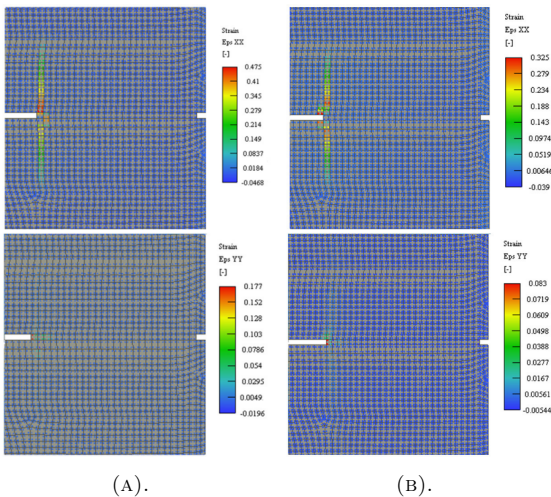


FIGURE 19. CT test simulation result of normal strains ε_{xx} and ε_{yy} at crosshead displacement of (A) 4.0 mm and (B) 5.0 mm with the pre-stress level of 3.3 MPa and critical load-grain angle of (A) $\theta_c = 0.4^\circ$ and (B) $\theta_c = 1.4^\circ$.

(Figure 19A bottom) or crack across the grain for $\theta_c = 1.4^\circ$ (Figure 19B bottom). This crack pattern is considered to correspond well with the failure type F0 shown in Figure 6A. All the load-displacement curves (Figure 18) reach the peak with respect to the pre-stress level. The post-peak behavior exhibits hardening, except for the calculation with 1.0 MPa in which softening occurs.

To summarize the CT test simulations with regard to critical load-grain angle θ_c and pre-stress level, different failures were observed:

- (i) type F0 occurred with $\theta_c = 1.6^\circ$ and the pre-stress level of 1.0 MPa and 2.1 MPa or with $\theta_c = 0.4^\circ$ and 1.4° and all the pre-stress levels of 1.0 MPa to 3.3 MPa,
- (ii) type F1 with $\theta_c = 1.6^\circ$ and 3.3 MPa,
- (iii) type F2-a with $\theta_c = 1.6^\circ$ and 3.0 MPa,
- (iv) type F2-b with $\theta_c = 1.6^\circ$ and 2.7 MPa.

The simulations with the pre-stress level of 2.7 MPa to 3.3 MPa and $\theta_c = 1.6^\circ$ reproduced well the peak load, post-peak behavior, and respective failure types F1 - F2 (Figure 16), that were observed in three experimental results out of five. Compared to it, the simulations with the same pre-stress level range and $\theta_c = 0.4^\circ$ or $\theta_c = 1.4^\circ$ reproduced adequately the load capacity, post-peak hardening, and respective failure type F0 (Figure 18), that were observed in two experiments out of five. Based on experimental and numerical results, the following recommendation was drawn up: to use $\theta_c = 1.6^\circ$ and $\theta_c = 1.4^\circ$ or less in 60% and 40% of pre-stressed CT test simulations, respectively, for a pre-stress level from the range between 2.7 MPa and 3.3 MPa.

Threshold angle θ_c , determined as the interval between 0° and 2° by visual assessment of off-axis tension specimens [3], may be regarded as one of timber material characteristics, which are typical for a significant variability. Thus, statistically significant results of not only off-axis tension tests but also CT experiments with regard to failure type are needed together with an appropriate statistical approach to numerical models.

7. CONCLUSION

The finite element method with an anisotropic constitutive model were used for numerical simulation of ASTM shear test and pre-stressed compact tension test. The numerical results reproduced adequately both the experimental responses and the crack patterns.

It was shown in shear test simulation that the value of the parameter f_{xy}^{ASTM} , obtained from $f_{xy}^{ASTM} = \frac{F_{max}}{A}$, represents the averaged stress at the failure plane, while the extreme stress locally experienced by the material is much higher. It is concluded that, if a finite element model of a structural member has a finer resolution of the stress field variation than is the size of the tested specimen, using the result of the ASTM shear test as the material strength may lead to underestimation of the member's load capacity.

The pre-stressed CT test simulation demonstrated the capability of the constitutive model to reproduce complex tensile-shear behavior of timber governed by tensile crack parallel or perpendicular to the grain or combination of both. The influence of the threshold principal load-grain angle θ_c to the results was analysed.

LIST OF SYMBOLS

A Shearing area [mm]
 c_1, c_2 Parameters of the t_n function [-]
 δ_n, δ_m Relative normal and tangent displacement [mm]
 $\delta_{m,crit}$ Shear displacement jump at which the cohesive traction diminishes to zero [mm]
 $\delta_{n,crit}$ Normal displacement jump at which the cohesive traction diminishes to zero [mm]
 $\Delta_{x,DIC}$ Relative vertical displacement by DIC [mm]
 E_x Modulus of elasticity along fibers [MPa]
 E_y Modulus of elasticity across fibers [MPa]
 f_{cx} Compressive strength along fibers [MPa]
 f_{cy} Compressive strength across fibers [MPa]
 f_{tx} Tensile strength along fibers [MPa]
 f_{ty} Tensile strength across fibers [MPa]
 f_{xy} Shear strength [MPa]
 f_{xy}^{ASTM} Shear strength according to standard ASTM [MPa]
 G_{xy} Shear modulus [MPa]
 l_{ch} Characteristic length of crack band model [mm]
 ν_{xy}, ν_{yx} Poisson's ratios [-]
 p Material parameter of the slope of the t_m function [-]
 F_{max} Maximum attained force [N]
 σ_{axial} Axial stress at failure for the off-axis test [MPa]
 σ_x, σ_y Normal stress along and across fibers [MPa]
 t_n, t_m Normal and tangent tractions [MPa]
 t_m^{ci} Crack-tangent traction at crack initiation [MPa]
 t_n^{ci} Crack-normal traction at crack initiation [MPa]
 τ_{xy} Shear stress [MPa]
 θ Principal load - grain angle [°]
 θ_c Threshold principal load - grain angle [°]

ACKNOWLEDGEMENTS

This work was supported by the Grant Agency of the Czech Technical University in Prague, grant No. SGS20/155/OHK1/3T/11.

REFERENCES

- [1] A. International. *ASTM D143-94, Standard Test Methods for small clear specimens of timber*. ASTM International, West Conshohocken PA, USA, 2000.
- [2] T. Sajdlová, P. Kabele. Finite element analysis of test configurations for identification of interface parameters in layered FRCC systems. In *HPFRCC-7: Proceedings of the 7th RILEM Workshop on High Performance Fiber Reinforced Cement Composites*, pp. 425–432. Stuttgart, Germany, 2015.
- [3] E. Šmídová, P. Kabele, M. Šejnoha. Material parameters of European spruce for tensile-shear fracture modeling. *Construction and Building Materials* [In preparation], 2021.
- [4] E. Smidova, P. Kabele. Constitutive Model for Timber Fracture under Tensile and Shear Loads. *Applied Mechanics and Materials* **784**:137–144, 2015. <https://doi.org/10.4028/www.scientific.net/AMM.784.137>.
- [5] C. B. Norris. Strength of orthotropic materials subjected to combined stresses. *Misc Pub FPL-1816 Madison, Wis : US Dept of Agriculture, Forest Service, Forest Products Laboratory* 1962.
- [6] A. Hillerborg, M. Modeer, P.-E. Petersson. Analysis of Crack Formation and Crack Growth in Concrete by Means of Fracture Mechanics and Finite Elements. *Cement and Concrete Research* **6**(6):773–782, 1976.
- [7] H. Reinhardt, H. Cornelissen, D. Hordijk. Tensile Tests and Failure Analysis of Concrete. *J Struct Eng* **112**(11):2462–2477, 1986.
- [8] E. Šmídová, P. Kabele, M. Šejnoha. Finite element simulation of single edge notched timber arch. *Journal of Computational and Applied Mathematics* p. 113676, 2021. <https://doi.org/10.1016/j.cam.2021.113676>.
- [9] J. Vorel, P. Kabele. Inverse analysis of traction-separation relationship based on sequentially linear approach. *Computers & Structures* **212**:125–136, 2019. <https://doi.org/10.1016/j.compstruc.2018.10.005>.
- [10] Ncorr downloads, <http://ncorr.com/index.php/downloads>, accessed 2021-6-13.
- [11] Ncorr_post: DIC post-processing tool, <http://mech.fsv.cvut.cz/~nezerka/DIC/index.htm>, accessed 2021-6-13.
- [12] *ASTM Standard E1820-09: Standard test method for determination of resistance to stable crack extension under low-constraint conditions*. ASTM International, West Conshohocken, 2010.